Mining, Metallurgy & Exploration
https://doi.org/10.1007/s42461-024-00957-9

Electrometallurgical Extraction of Silicon Using Solid Oxide Membrane—Molten Salt Electrolysis

Aditya Moudgal[1] · Mohammad Asadikiya[3] · Yu Zhong[2] · Adam C. Powell IV[2] · Uday Pal[4]

Received: 3 November 2023 / Accepted: 6 March 2024

Abstract
This paper describes a computational and experimental approach to electrodeposition of silicon using a MgF_2-CaF_2-CaO-Y_2O_3-SiO_2 molten salt electrolyte and a yttria-stabilized zirconia solid oxide membrane at the anode. A secondary and tertiary current density distribution model shows anodic current density between 0.5 and 1 A cm^{-2} with a fairly even distribution along the anode surface except at the ends of the anodes. Finite element analysis of industrial cell magnetohydrodynamics (MHD) shows electrolyte flow to be 23 times slower compared to a calculated analytical model. The experiments demonstrate formation of highly pure silicon in the melt with particle sizes ranging from a few µm to clusters of 2 ~ 3 mm. Finally, the mechanism of Si formation based on a short thermodynamic analysis was discussed.

Keywords Silicon · Electrometallurgy · Electrodeposition · Molten salts · Numerical modeling

1 Introduction

Silicon is an important industrial element that has seen widespread usage and adoption in the solar, electronic, and metallurgical industries. It plays an important role especially in the solar industry where polysilicon and mono-silicon-based solar cells dominate the market due to their abundance of availability, low cost, and efficiency [1]. Conventionally, high-purity solar-grade silicon is manufactured using the Siemens process. Silicon modules are known to last long ~ 25 years and retain 80% of their original efficiency [2]. But today's polysilicon industry is extremely energy-intensive, consuming 300 kWh kg^{-1} silicon, and its use of hazardous chlorosilanes has resulted in multiple fatal accidents in recent years. It also emits CO_2 during the first carbothermic reduction step [3]. Therefore, having a clean, safe, cost-competitive source of silicon could advance lower costs and even wider usage of solar technology. Combined with uncertainty and volatility in silicon prices, newer methods of refining silicon to solar grades need to be explored [3–5].

✉ Adam C. Powell IV
acpowell@wpi.edu

1 Idaho National Laboratory, Idaho Falls, ID, USA
2 Worcester Polytechnic Institute, 100 Worcester Rd., Worcester, MA 01609, USA
3 SilarTek, Inc., Leominster, MA 01453, USA
4 Boston University, 15 St. Mary's St., Boston, MA 02215, USA

Currently, to produce solar grade silicon, 99.8% pure silica is carbothermically reduced to form metallurgical-grade silicon which is about 98% pure using the following reaction:

$$SiO_2 + C \rightarrow Si + CO_x$$

This metallurgical-grade silicon is further refined into solar-grade silicon by the conventional Siemens process which involves hydro-chlorination using hydrochloric acid, followed by distillation to form purified trichlorosilane which is an intermediate product then deposited by chemical vapor deposition in bell jars onto high-purity polysilicon filaments [6]. Hydrogen chloride is formed as a by-product of this reaction. As noted, this process is energy intensive and needs critical temperature control to get high-purity uniform deposits. Also, this process is a batch process. Another popular process is the fluidized bed approach which is continuous and also can be done at a lower temperature of 750 °C. Silane gas is reduced to pure silicon and deposited on the surface of silicon seeds in a fluidized bed reactor. These seeds are removed from the bottom of the reactor to give high-purity silicon which requires further processing before being used in solar cells [7].

Both these processes use unsafe halogenated compounds, produce CO_x along the supply chain, and consume large amounts of energy. The carbon reductant also introduces considerable impurities into the silicon product. Therefore, alternative methods such as electrodeposition using liquid salts are being explored [8–11]. Electrodeposition of silicon using molten

Published online: 03 June 2024

chlorides, molten fluorides, and mixed chlorides and fluorides has been studied in the past. Though a considerable amount of work has been done, large-scale production has not been practically achieved using liquid salts. The challenge also remains of preventing salt trapping in dendrites during electrodeposition.

An innovative method that has been previously proven in the direct single-step reduction of metals from oxides is solid oxide membrane (SOM) electrolysis [12–15]. The solid oxide membrane used in these processes is a yttria-stabilized zirconia (YSZ) membrane similar to that used in a solid oxide fuel cell. A novel flux developed by Villalón et al. [16] at Boston University shows promise in depositing high-purity silicon in a single step. The flux contains a CaF_2-MgF_2 eutectic with CaO, Y_2O_3, and SiO_2. This flux has a high ionic conductivity, low viscosity, and high solubility of silica due to formation of Si-O-F complex anions at 1100 °C [17]. It has been previously used to deposit silicon using a liquid tin and molybdenum cathodes. The challenge lies in getting a high-density deposit using a solid cathode towards direct application in this system. Towards these goals, macroscopic finite element modeling and experiments have been carried out and reported in this article.

2 Macroscopic Cell Modeling

Electrolysis cell modeling is done using COMSOL multiphysics, and the modules used are electrochemistry (ec), transport of diluted species (tds), and laminar flow (spf) [18]. The primary goals of the model are to understand the current density distribution involving charge and mass transfer and magnetohydrodynamics (MHD) of the electrolyte to enable better cell design. These modules mentioned have the requisite predefined couplings to simulate the most significant effects to understand the dynamics of the salt and behavior of the cell. The primary current density (ohmic resistance) of the cell has previously been described in Moudgal et al. [19].

2.1 Governing Equations

This article describes secondary and tertiary current density distributions, i.e., current density that involves charge and mass transfer. The secondary current density distribution is a combination of the electrolytic resistance and activation overpotential of the cell [20]. The activation overpotential is governed by the Butler-Volmer equation at the electrode-electrolyte interface. The tertiary current density distribution is governed by ohmic polarization, activation polarization, and concentration polarization. Concentration polarization is change in species concentration on the electrode surface and electrolyte during the duration of electrolysis, and depends strongly on electrolyte flow conditions.

The primary current density is modeled based on the Ohm's law for both the electrode and electrolyte which is given by

$$J = -\sigma \nabla \phi \ with \ current \ conserved \nabla \cdot J = Q \tag{1}$$

where σ is the electrolyte conductivity, J is the flux, and ϕ is the potential. In the primary current density, the local potential at the anode and cathode is equal to the potential of the electrolyte next to each electrode, and Q is charge density change.

The secondary current density is similar to the primary current density in that Ohm's law is used to model the solution resistance and resistance of the electrodes as described in Eq. 1, but the electrode-electrolyte interface resistance is governed by a standard equation that describes electrode kinetics such as the Butler-Volmer equation or Tafel equation. In this article, we model the interface using the Butler-Volmer equation [21]. The electrode-electrolyte interface is given by

$$\eta = \phi_{\text{electrode}} - \phi_{\text{electrolyte}} - E_{\text{eq}} \tag{2}$$

where η is the overpotential, $\phi_{\text{electrode}}$ and $\phi_{\text{electrolyte}}$ are the potential of the electrode and electrolyte, respectively, in volts, and E_{eq} is the equilibrium potential also in volts.

The charge transfer is denoted by

$$i = i_0 \left(e^{\frac{\alpha \ (anode), F\eta}{RT}} - e^{\frac{\alpha \ (cathode), F\eta}{RT}} \right) \tag{3}$$

where i is current density (A m^{-2}), i_0 is the exchange current density (A m^{-2}), α (anode) and α (cathode) are the symmetry factors for the anode and cathode, F_η is the faradaic overpotential, R is the universal gas constant (J K^{-1} mol^{-1}), and T is the temperature (K).

The electrolyte in the tertiary current density distribution is governed by the Nernst-Planck equation, an extension of the Fick's law. Diffusivity and species concentration both affect the cell in the tertiary current density distribution. The electrodes still follow Ohm's law. The current density of the electrolyte is described by

$$i_l = F \ \Sigma_i^n z_i \left(-D_i \nabla c_i - z_i \ u_i F c_i \nabla \phi_{electrolyte} \right) \tag{4}$$

with current conserved $\nabla i_l = Q_l$ where i_l is the current density of the electrolyte, F is Faraday's constant (C mol^{-1}), z_i is the charge number of species i, D_i is the diffusion coefficient of species i (m^2 s^{-1}), c_i is the concentration of ions of species i (mol m^{-3}), and u_i is the mobility (velocity vector) of species i (S mol kg^{-1}).

The electrolyte neutrality is maintained by

$$\Sigma_i z_i c_i = 0 \tag{5}$$

The electrolyte-electrode current density expression is shown below

$$i = i_0 \left(e^{\frac{\alpha \ (anode), F\eta}{RT}} - e^{\frac{\alpha \ (cathode), F\eta}{RT}} \right) \tag{6}$$

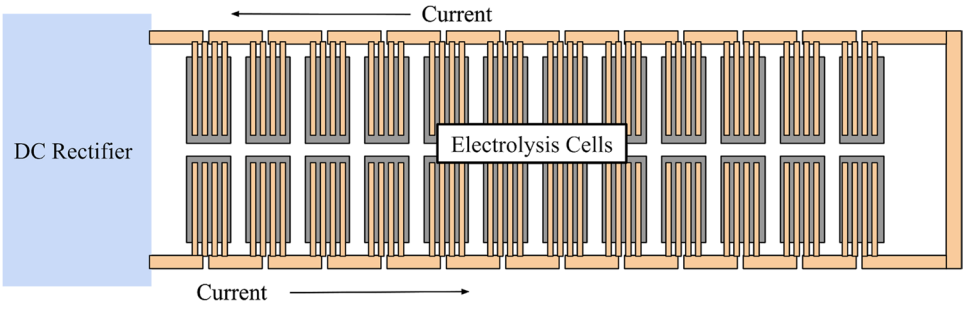

Fig. 1 Arrangement of cells in an envisioned 300 kA plant

where C_{red} and C_{oxy} are the concentrations of the reduced and oxidized species, respectively.

These current densities thus calculated can tell us the nature of the deposit. An even current density along the anode or cathode predicts a uniform deposit.

The MHD effect is described using a combination of Maxwell's equations with the Navier-Stokes equations including the Lorentz force. It describes the flow of the electrolyte in a magnetic field since the electrolyte is ionically conductive. Considering an external magnetic field B_0 due to the flow of current through the conductor, the total field acting on the electrolyte is

$$B = B_0 + b \tag{7}$$

The conservation equations of the Navier Stokes equations with the Lorentz force that is generated are

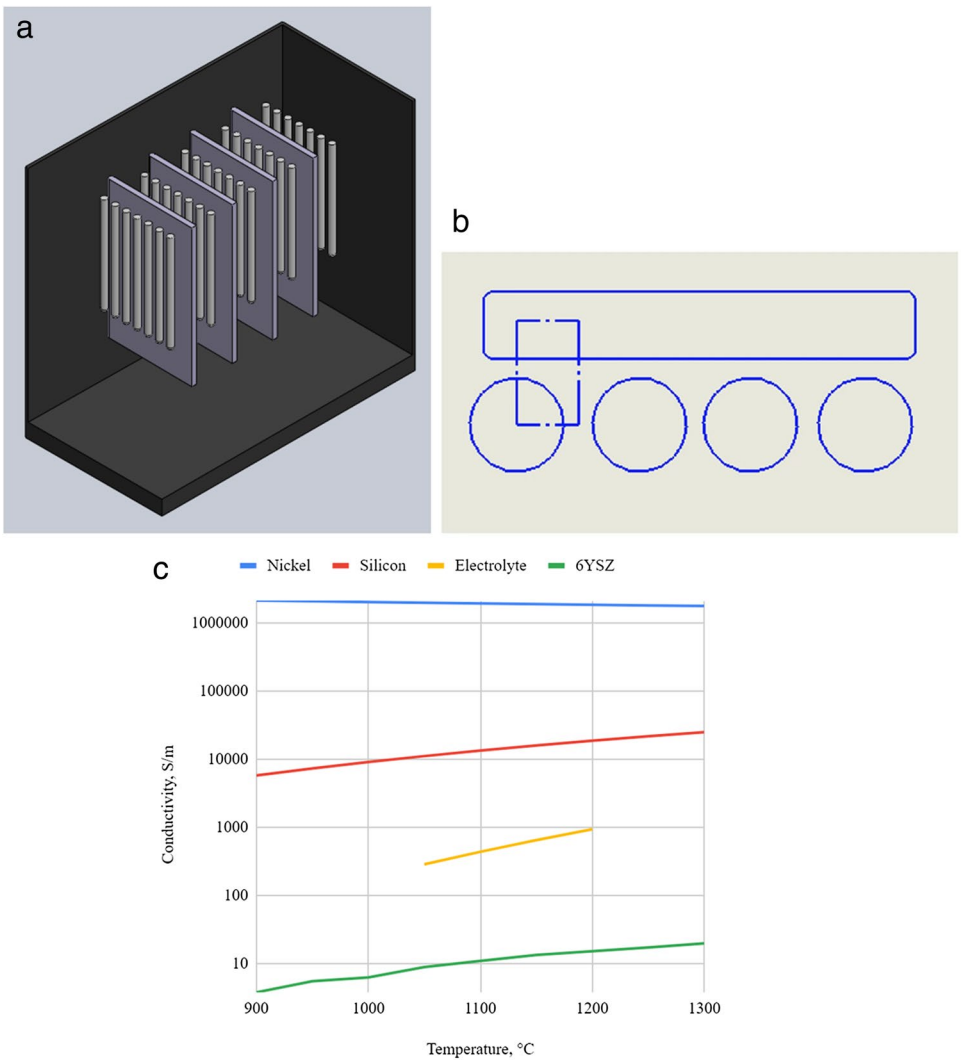

Fig. 2 **a** Close-up view of anode and cathode arrangement. **b** Primitive unit cell used for modeling. **c** Temperature-dependent electrical conductivities of cell materials

Fig. 3 Experimental setup of cell

Table 1 Initial bath composition using YF_3 and Y_2O_3

Salt	Original %	Modified %
MgF_2	39.74%	39.74%
CaF_2	49.76%	52.97%
CaO	4.00%	1.69%
YF_3	4.00%	
Y_2O_3		3.10%
SiO_2	2.50%	2.50%

$$\frac{\partial v}{\partial t} + (v.\nabla)v = -\frac{1}{\rho}\nabla p + \nu\ \nabla^2\ v + \frac{1}{\rho}\ \left(j \times B_0\right) \tag{8}$$

$$\text{with} \nabla \cdot v = 0 \tag{8}$$

Combining the above equations with Maxwell's equations and Ohm's law, we get

$$J = \sigma\ (E + u \times B) \tag{9}$$

$$\text{and } F = J \times B \tag{10}$$

2.2 Current Density Model Geometry

The cell geometry depicted here is done considering a cell in a potline with a 300 kA current bus. Figure 1 shows the layout of the cells in what is envisioned to be a silicon plant. The cells are considered to have cylindrical anodes and slab cathodes as depicted in Fig. 2a. The modeling geometries consider (1) a primitive cell consisting of half the thickness of the cathode and one quarter of a single anode and (2) a larger geometry with three anodes surrounded by electrolyte. This is done to save on computation time. Temperature-dependent conductivities of the cell materials taken from literature are shown in Fig. 2c. The relatively higher conductivity of silicon and nickel shows that electrical resistance of the solid and liquid electrolytes (YSZ and CaF_2-MgF_2 eutectic molten salt) mostly limit cell current density distribution.

3 Experimental Method

Figure 3 below shows the apparatus for SOM electrolysis of silicon. The setup consists of a stainless steel crucible coated with boron nitride, a silver anode with a graphite current collector inside a YSZ membrane rod closed at one end, and a silicon wafer cathode with a 304 stainless steel current collector. The silicon wafer was attached to the stainless steel current collector mechanically by inserting the wafer into a slit machined using a wire electric discharge machine and held tightly by stainless steel screws. The setup is enclosed in a 310 stainless steel tube and suspended in a furnace. The process operating temperature is between 1100 and 1150 °C. Argon or Ar-H_2 forming gas is continuously passed through the system to maintain an inert environment and prevent the reaction of oxygen with the molten salts and silicon. The cell is run potentiostatically using a DC power supply.

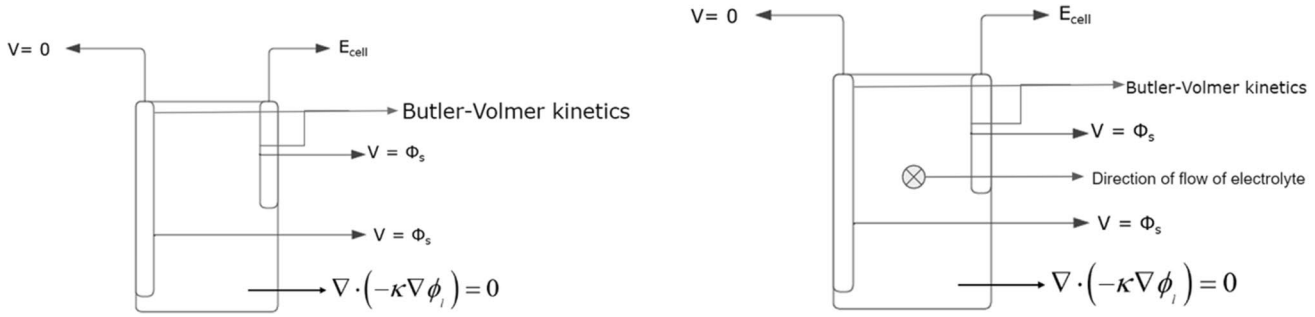

Fig. 4 Boundary conditions for secondary and tertiary current distribution

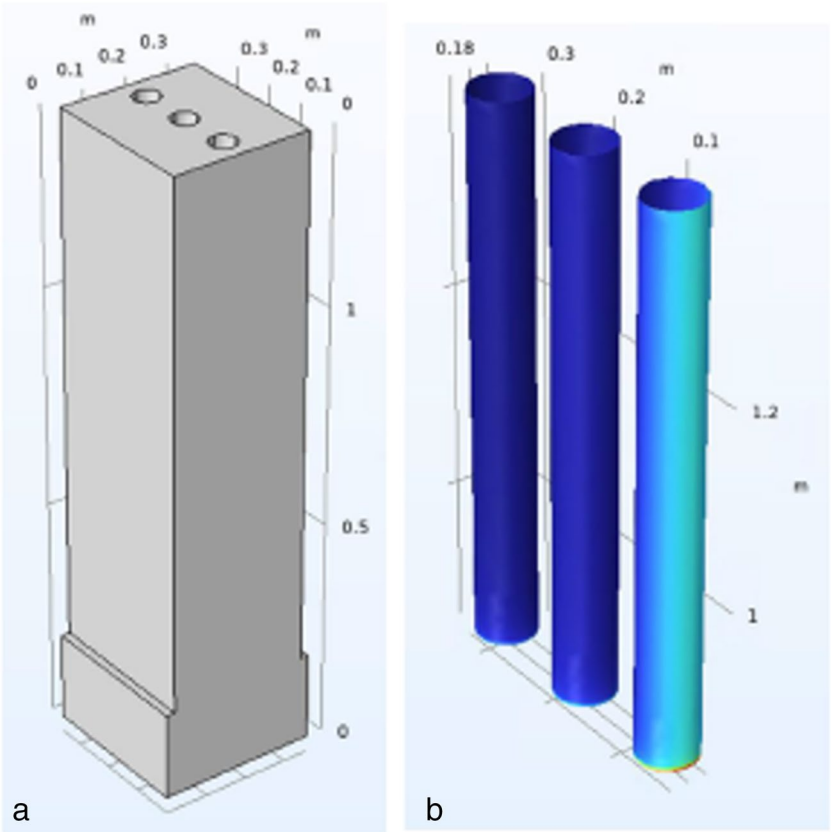

Fig. 5 **a** Geometry and **b** secondary and tertiary current density

Based on the work by Villalón on flux properties [16], the initial composition of the flux using either Y_2O_3 or YF_3 is shown below in Table 1. Based on experimental results, the bath composition was changed and this is described in Sect. 4.

4 Results and Discussion

4.1 Secondary and Tertiary Current Density Distribution

Figure 4 below shows the boundary conditions that have applied to the secondary and tertiary current density distribution. The cathode-electrolyte interface is governed by the Butler-Volmer kinetics in secondary current density and a combination of secondary and concentration polarization in the tertiary as mentioned previously. The change in concentration of the electrolyte is due to flow which is dependent on the magnetic field due to the flow of current in the electrodes. The direction of flow is dependent on the direction of the magnetic field and is into the plane depicted by the cross symbol. The conductivity of silicon was taken to be 1.87×10^4 S m^{-1} [22].

Figure 5 depicts the secondary and tertiary current density for a pair of distinct geometries considering three anodes based on the boundary conditions mentioned. The current density appears to be evenly distributed over the surface, but it is primarily high at the bottom of the SOM tube.

4.2 Magnetohydrodynamics

An analytical resolution to the Lorentz force was established and compared with the model derived from COMSOL software. This analytical computation showed the ionic velocity to be six orders of magnitude more elevated than the corresponding value derived from the COMSOL model.

The Lorentz force is first determined by calculating the magnetic field strength. The principal distribution contributes a current density of 0.5 A cm^{-2}. The magnetic field strength associated with this current density, positioned 1 m away from the conductor immersed in the electrolyte, can be computed using the following expression:

$$B = \left(\mu_0 \times I\right)/(2\pi r)$$

where "B" represents the magnetic field strength, "I" denotes the total current through the cell (300 kA), "r" is the distance from the conductor, and "μ_0" corresponds to the permeability of free space. The given parameters are $r = 2.7$ m and $\mu_0 = 4\pi \times 10^{-7}$ T m A^{-1}. Upon inserting these values into the above equation, we get:

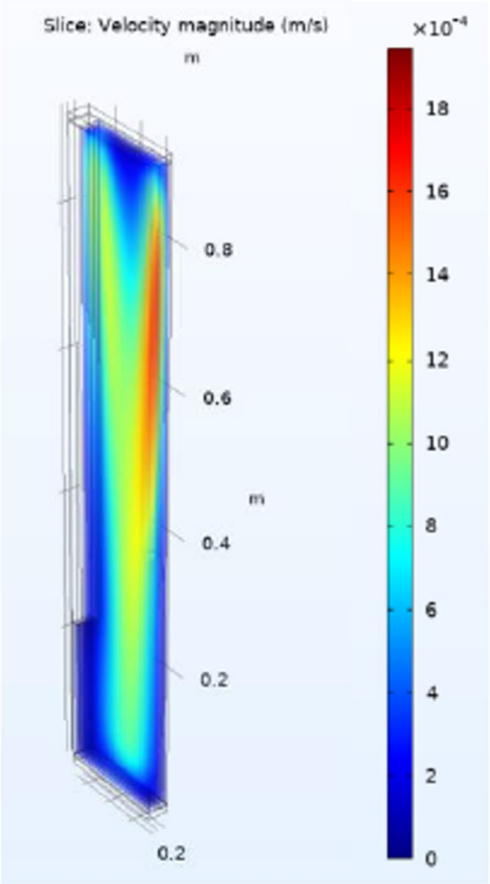

Fig. 6 COMSOL simulation showing velocity of electrolyte

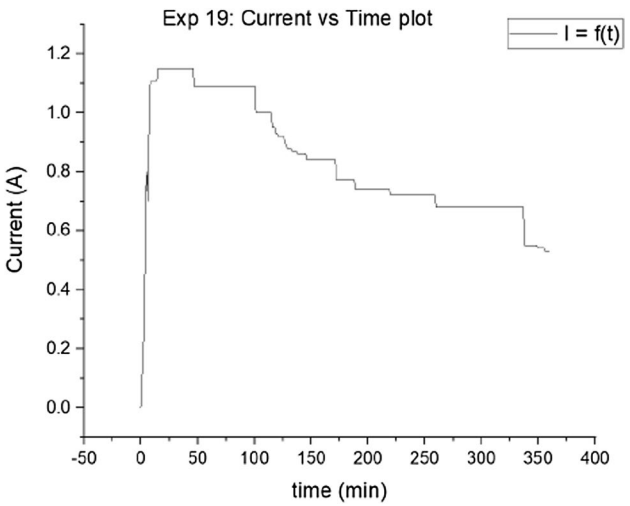

Fig. 7 Measured current vs time plot showing a current of approx ~ 1 A passing through the cell

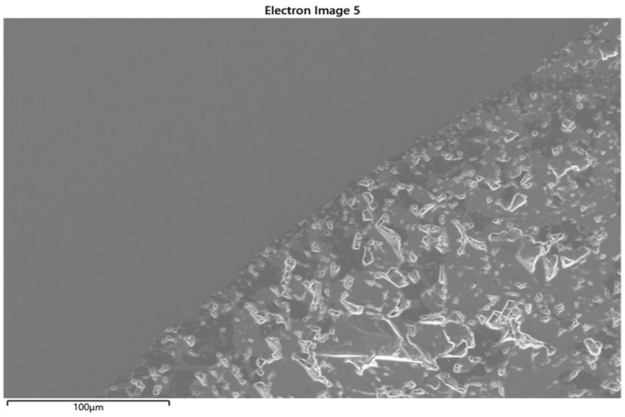

Fig. 8 SEM image after electrolysis

$$B = \left(4\pi \times 10^{-7}\ T\ m\ A^{-1}\right) \times (300,000\ A)/(2 \times \pi \times 2.7\ m) = 0.0223\ T$$

Consequently, the magnetic field emanating from the conductor on the opposite side, situated 8.1 m away, results in a field strength of 7.41×10^{-3} T. Hence, the total field strength equates to 0.0291 *T*.

Given these parameters, the magnetic field strength sums up to approximately 0.0291 *T*. Utilizing the derived values of the magnetic field strength and electric current density of 0.5 A cm^{-2}, the Lorentz force "*F*" can be calculated by the formula:

$$F = J \times B$$

where $B = 0.0291\ T$ and $J = 0.5$ A cm^{-2}. By substituting the above values, we get:

$$F = (0.0291\ T) \times \left(5000\ A\ m^{-2}\right) = 145.5\ N\ m^{-3}$$

Therefore, the Lorentz force acting on the conductor is approximately 145.5 N m^{-3}.

We can approximate flow between electrodes using the solution for fully developed laminar flow between parallel plates at the center of the cell, which is:

$$u = \frac{B_i}{\mu}\left[\frac{h^2 - y^2}{2}\right]$$

Substituting $B_i = 0.0291T$, viscosity = 3.5 mPa s, distance between the anode-cathode being 10 cm, and velocity calculated at the center, we get the value for velocity to be

$$0.0415\ m \cdot s^{-1}$$

This is approximately ~ 23 times higher than the model shows us. Much of this discrepancy is likely because the active anode area is a small fraction of the cathode area, which would reduce the average current density.

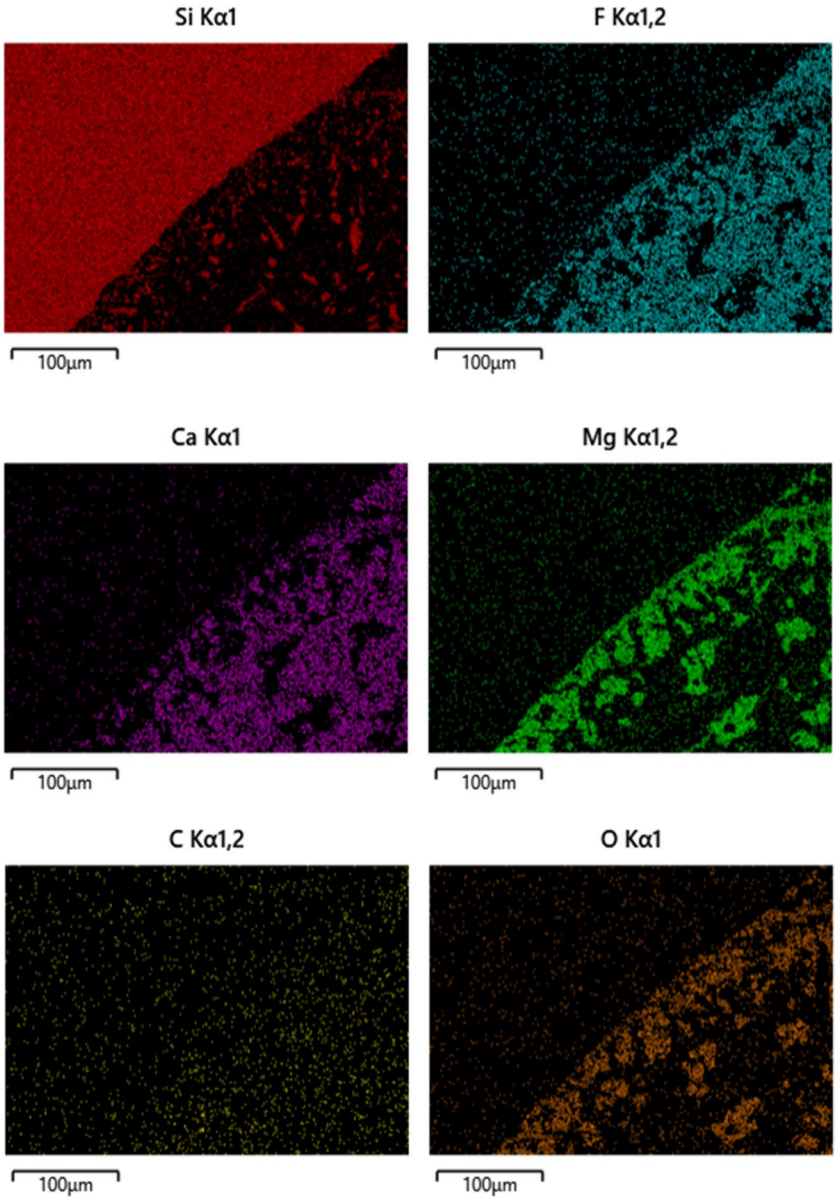

Fig. 9 EDS scans of Fig. 8 showing pure Si in melt and MgO in the flux

Table 2 Flux composition with the elimination of CaO and Y_2O_3

Salt	wt%
MgF_2	43.25%
CaF_2	49.62%
CaO	0%
Y_2O_3	0%
SiO_2	11.56%

It is noteworthy that the maximum flow velocity registered in the COMSOL model is observed proximate to the cell's anode, at a scale of 1.8 mm s^{-1} (Fig. 6).

4.3 Experiments

In the initial experiments, small islands of pure silicon were seen in the melt near the cathode, but no silicon deposits were observed attached to the cathode, indicating that the experimental conditions or parameters may require further optimization or reconsideration. The current vs time plot for experiment 19 which is a long duration electrolysis is shown below in Fig. 7. Figure 8 shows an SEM image of the flux-wafer interface. Figure 9 shows composition maps, indicating there are islands of pure silicon in the bath adjacent to the cathode, but indicates the presence of MgO at the cathode-electrolyte

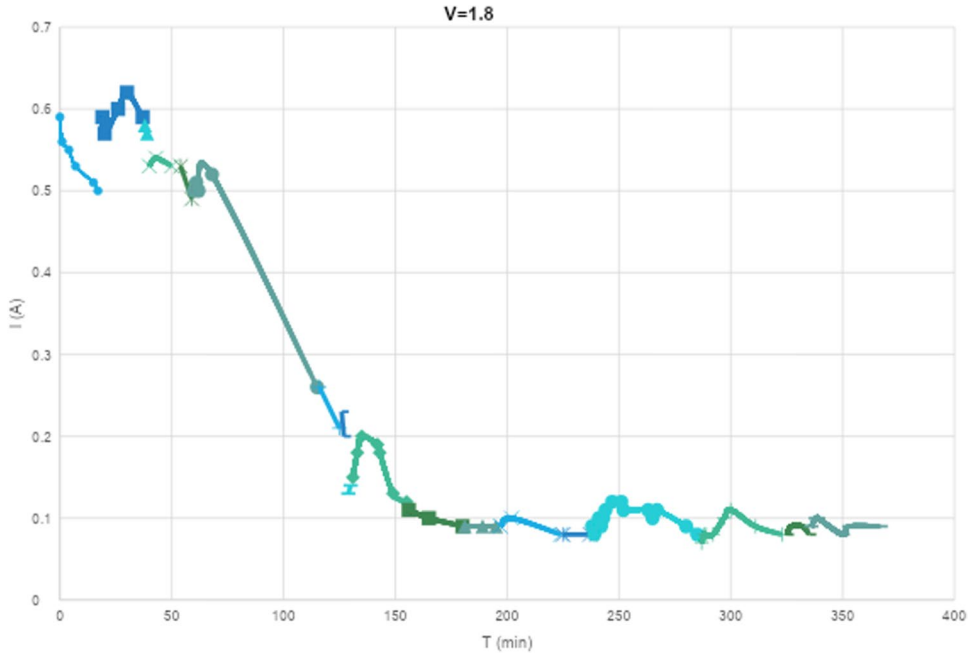

Fig. 10 Current vs time plot for CaO and Y_2O_3 free flux. The potential of the cell V is 1.8 V. The anode was rotated at certain intervals to promote better mixing and mass transfer

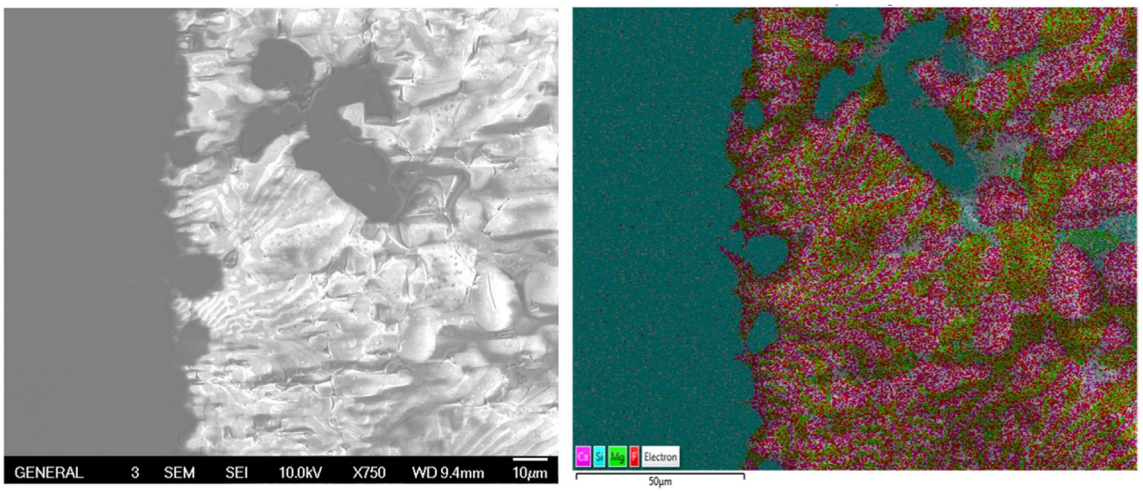

Fig. 11 SEM image and EDS compositional map of electrolyte-cathode interface after electrolysis

interface and in the bath. Several factors could be responsible for the absence of silicon deposits in these experiments, including the electrolyte composition, applied voltage, cathode material, or the presence of impurities. It is possible that the chosen molten salt did not provide sufficient ionic conductivity or that the silicon ions were hindered from migrating towards the cathode. Alternatively, the experimental conditions may have promoted some side reactions, and mass transfer limiting conditions preventing silicon deposition.

To overcome the challenges of MgO passivation, several thermodynamic calculations and experiments were performed and the composition of the flux was changed. Initially, the oxide content of the flux was reduced by elimination of CaO and Y_2O_3, but the silica content was increased to promote

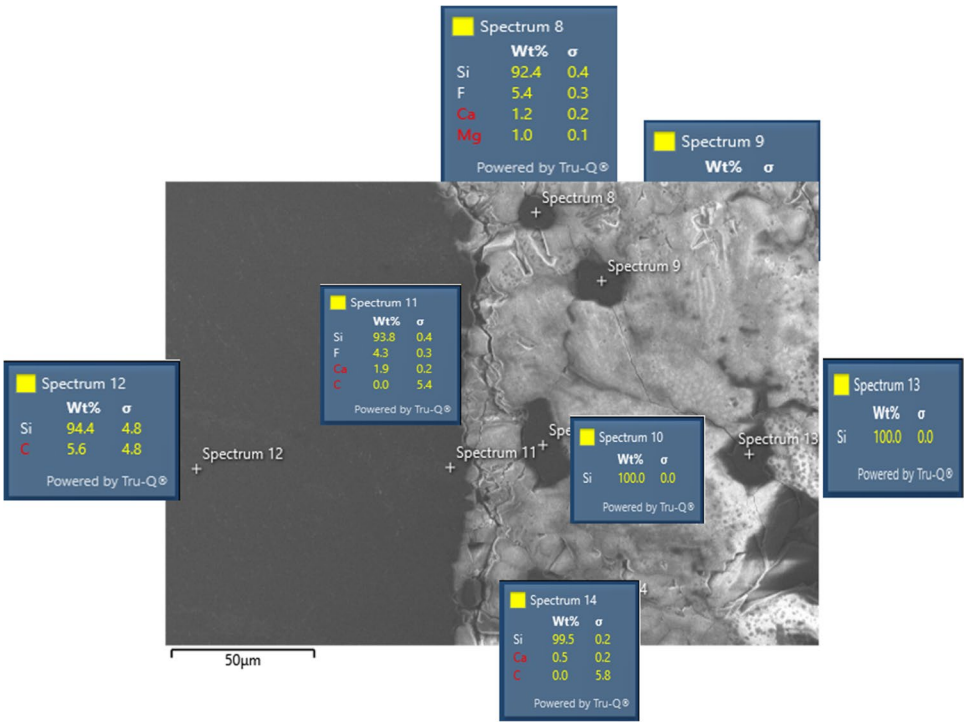

Fig. 12 EDS point scan showing composition after electrolysis

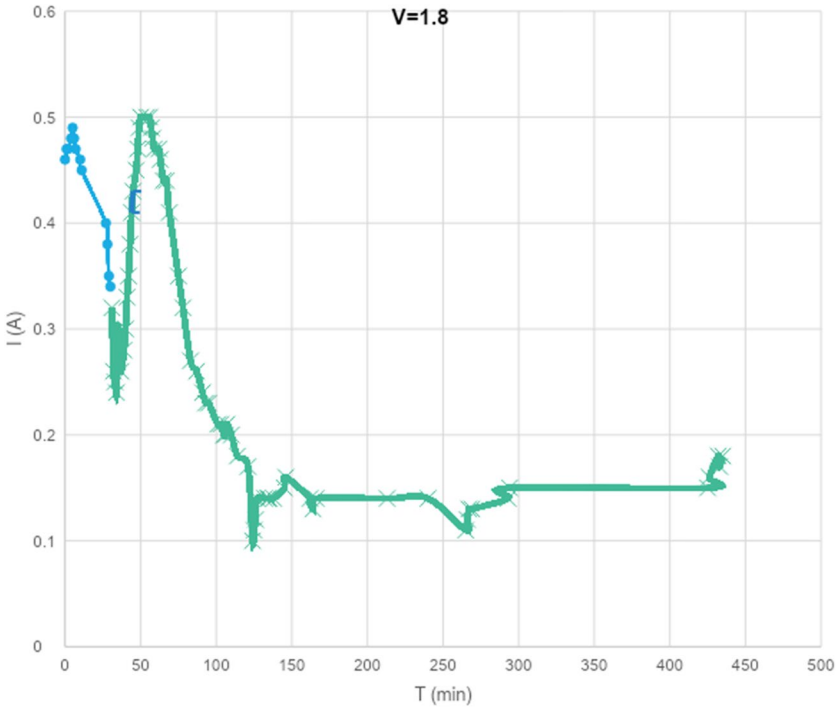

Fig. 13 Current vs time plot (unit: V) showing a decrease in current over a short period of time indicated lower viscosity. The second peak indicates rotation of the cathode to promote mass transfer

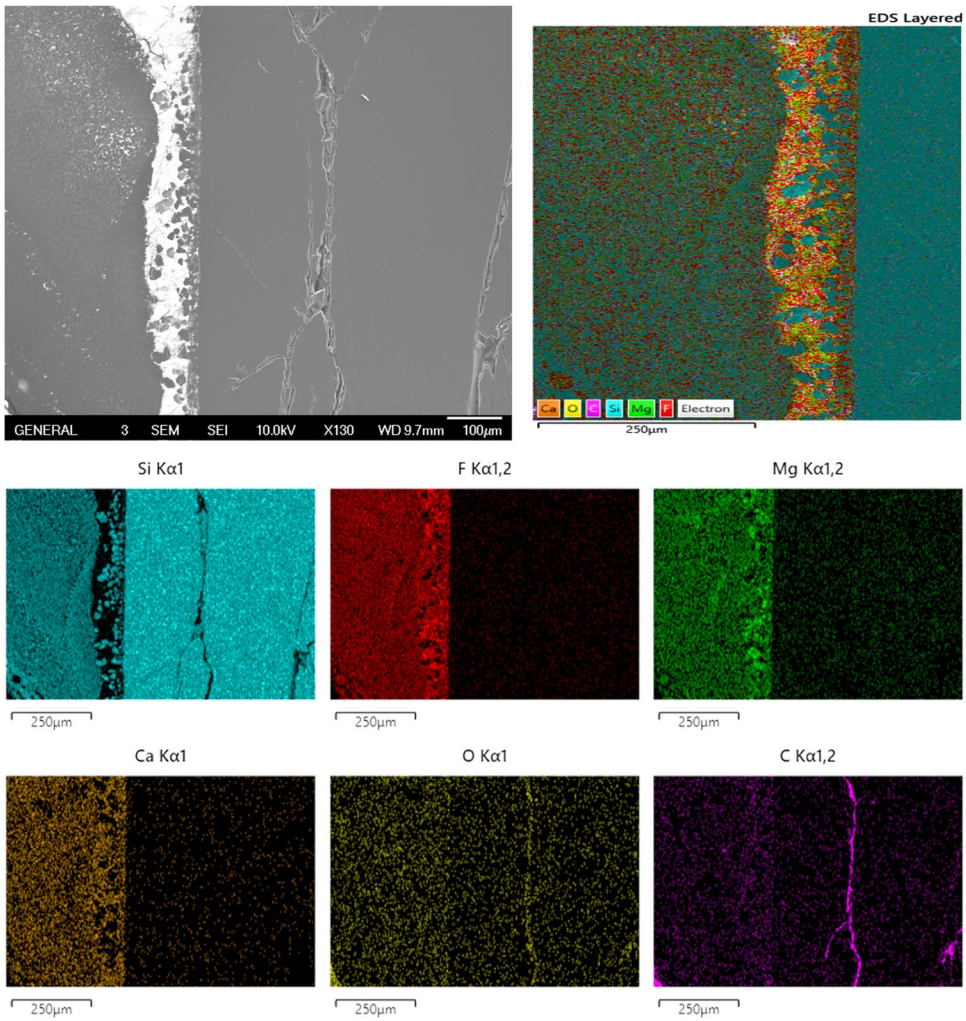

Fig. 14 SEM and EDS scans showing formation of larger particles of silicon

availability of silicon ions and the composition of the flux is shown below (Table 2).

This flux composition was melted and electrolyzed using a carbon anode. The current vs time plot for this composition is shown in Fig. 10.

The SEM images and EDS point scan shown in Figs. 11 and 12 show that there is silicon formation but the time taken for the current to drop still indicates a flux that is highly viscous.

To eliminate high viscosity, the flux composition was further changed by reducing the amount of silica further eliminating oxide ions in the melt.

Salt	wt%
MgF_2	47.21%
CaF_2	50.42%
CaO	0%
Y_2O_3	0%
SiO_2	2.35%

The current against time plot is shown in Fig. 13 below for the flux composition.

This flux composition also resulted in formation of silicon, but on further analysis, it was observed that the flux was still highly viscous from the current vs time plot. To further lower viscosity, an experiment with an optimal amount of CaO and SiO_2 was done (Fig. 14). The flux composition was as follows:

Salt	wt%
MgF_2	51.7%
CaF_2	40.9%
CaO	4.91%
Y_2O_3	0%
SiO_2	2.56%

In this flux composition, the amount of CaO to be added to the flux to reduce viscosity was calculated considering the thermodynamics of the system. The initial thermodynamic calculations were done

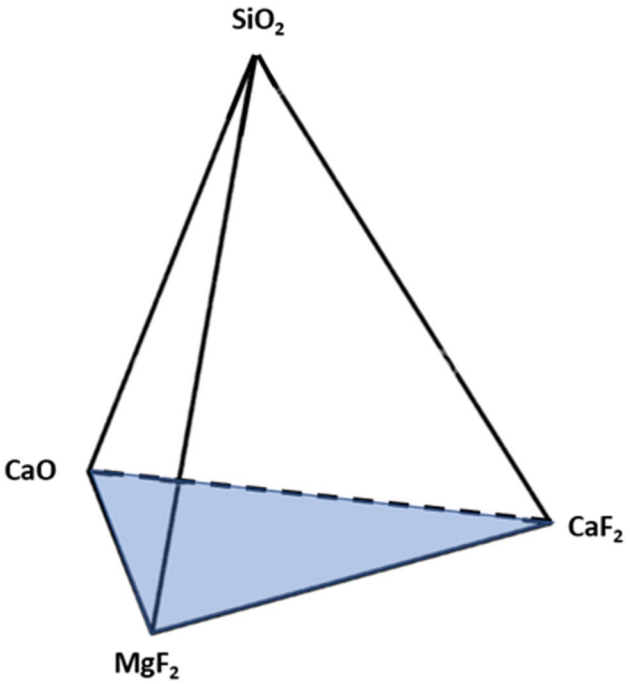

Fig. 15 System components along with SiO_2 precursor. The shaded region indicates initial region considered in Thermo-Calc

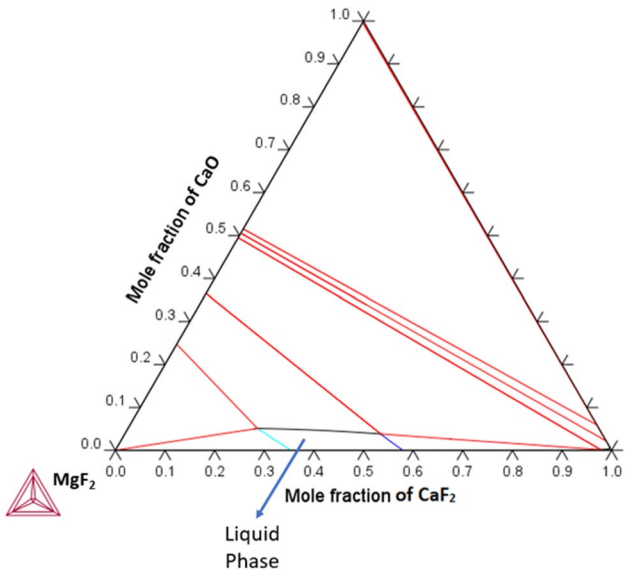

Fig. 16 Calculated phase diagram of MgF_2-CaF_2-CaO at 1073 °C

using the CALculation of PHAse Diagrams (CALPAD) approach. CALPHAD is a computational thermodynamic approach which has proven to accelerate material design and reduce experimental trial and error attempts [23–25]. Initial calculations checked if the electrolyte was completely liquid at the electrolysis temperature. This was done using Thermo-Calc and the TCOX11 database, an inbuilt option in the software which is mainly for oxides [26, 27]. The system considered did not include Y_2O_3 shown in Fig. 15 below.

In the intended experiments, the electrolysis bath components of MgF_2-CaF_2-CaO are expected to be fully liquid before adding SiO_2. An initial plot of this at a temperature of 1073 °C shows us the region of the liquid phase in Fig. 15.

The liquid region was replotted as shown in Fig. 16, and this showed that the maximum mole fraction of CaO which can be added without forming MgO during electrolysis is 0.05 at the MgF_2-rich side and slightly less than 0.04 at the CaF_2-rich side. Based on Villalon et al. [16], CaF_2 activity has an effect on SiF_4 which removes Si from the bath (Fig. 17). Therefore, moving towards the MgF_2-rich side was determined to combat MgO passivation.

Based on these calculations and the flux composition, the flux was melted and electrolyzed using a carbon anode. The current vs time plot is shown below in Fig. 18.

As observed, we see a far more stable current indicating a lesser viscosity in the flux. The cathode was also rotated during this experiment. Rotating the cathode promotes local electrolyte movement which in turn increases mixing of species, a higher mass transport, reduced thickness of the diffusion layer, a higher current density, and lower overpotential. The SEM images and the EDS scans shown below in Fig. 19 show an even formation of silicon in the flux, but we still observe some formation of MgO.

5 Conclusions

The role of secondary and tertiary current density distribution has been found to be important in deciphering the complex nature of the electrolysis process. The current density was found to be in the range of 0.3 ~ 0.7 A cm^{-2}. This can be aimed towards improving electrolytic cell design, adjustment of electrode geometry, and modification of electrolyte composition, all aimed towards improving cell efficiency and the quality of the resultant silicon deposition process.

The MHD model in correlation to the viscosity observations of the electrolyte tells us that we need more viscosity data to better understand the melt at these temperatures.

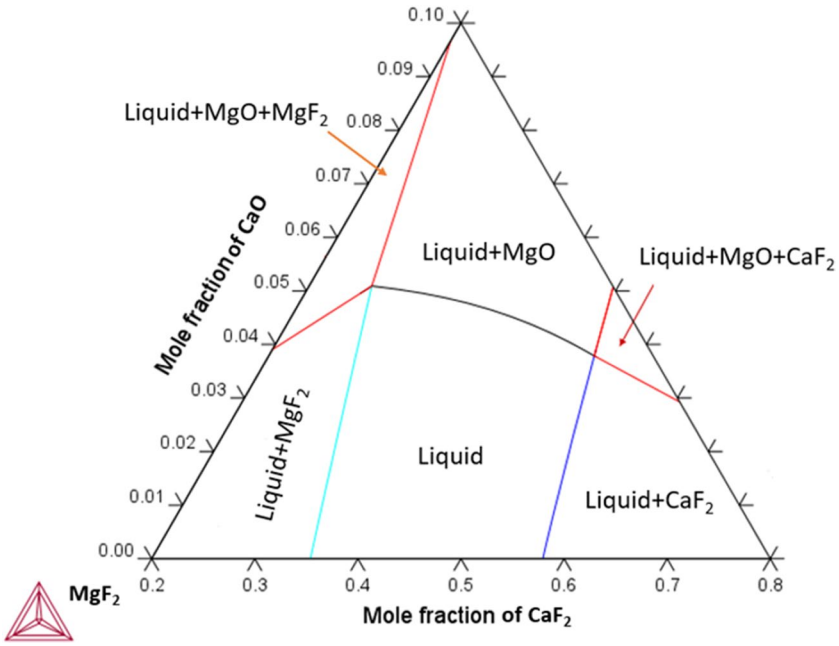

Fig. 17 Phase diagram of specific composition range in the MgF_2-CaF_2-CaO ternary

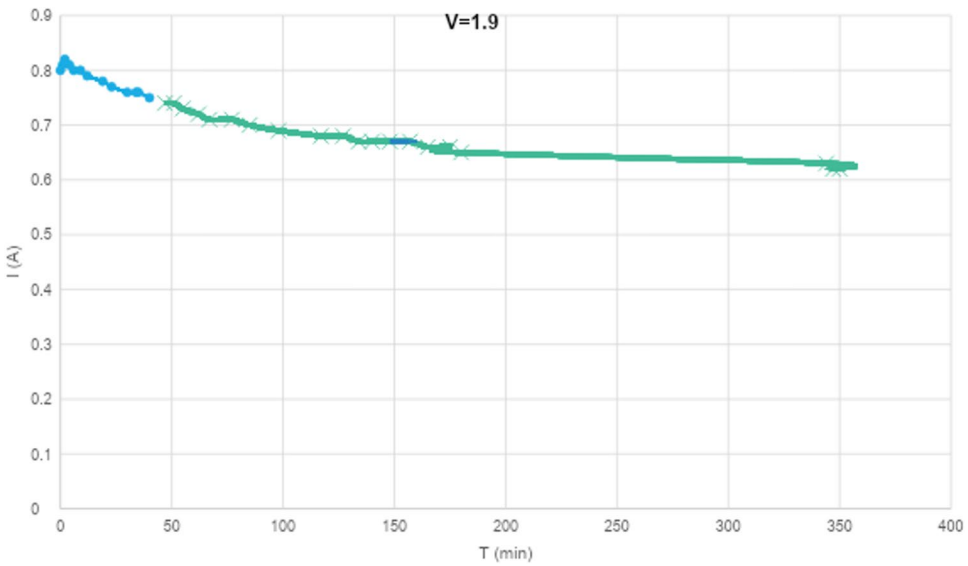

Fig. 18 Current vs time plot with a modified flux composition containing CaO

MgO passivation is observed, and changing the flux composition has shown us that pure silicon is formed in the melt. Further improvement in these parameters will lead to growth of silicon on the cathode.

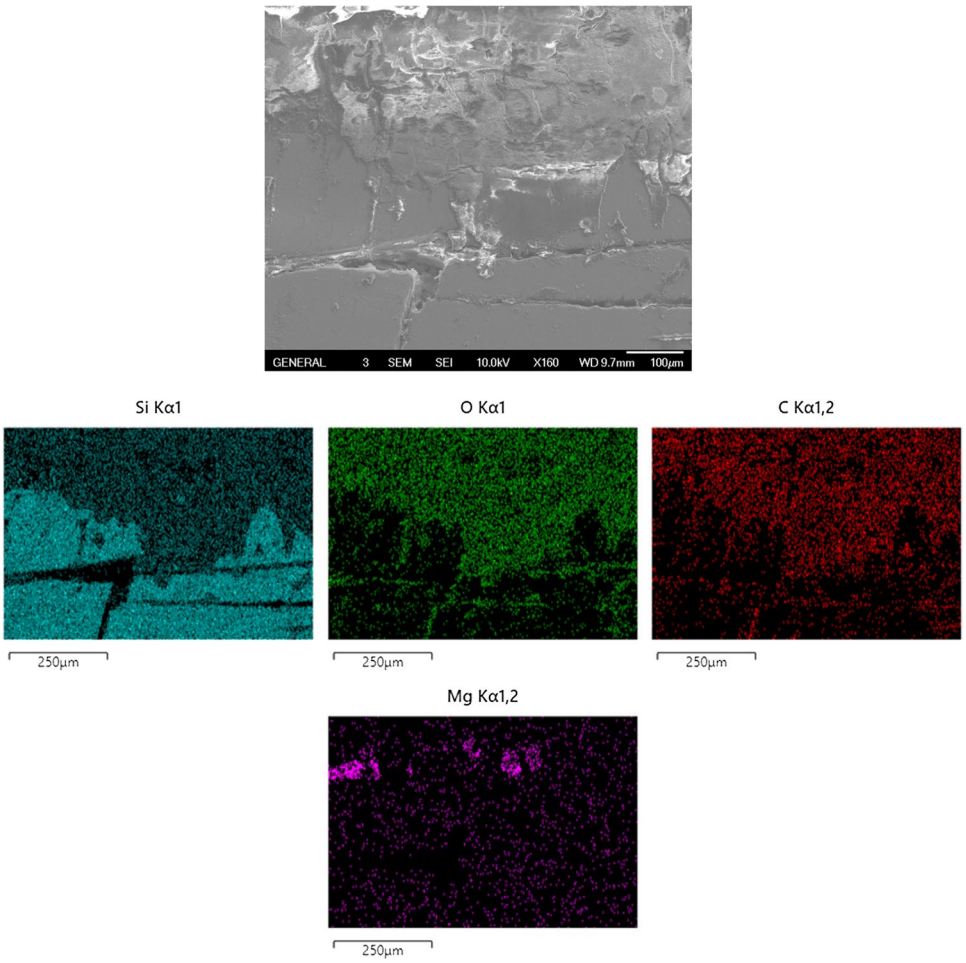

Fig. 19 SEM and EDS scans showing even distribution of silicon in flux with trace amounts of MgO formation

Supplementary Information The online version contains supplementary material available at https://doi.org/10.1007/s42461-024-00957-9.

Acknowledgements Aditya Moudgal would like to thank Anurag Bhattacharjee (WPI) for useful discussions. This material is based upon work supported by the US Department of Energy's Office of Energy Efficiency and Renewable Energy (EERE) under the Solar Energy Technologies Office Award No. DE-EE0008988 and by the US National Science Foundation under Award Nos. 1937818 and 1829089. This research was performed using computational resources supported by the Academic and Research Computing group at Worcester Polytechnic Institute.

Data Availability Data cite in this article will be made available upon request to the corresponding author.

Declarations

Conflict of Interest Asadikiya, Powell, and Zhong are part owners of SilarTek, LLC which is working on commercializing this silicon extraction technology. Pal is an inventor of US Patent 10,266,951 which describes part of this silicon extraction technology. Powell is an inventor of US Patents 8,460,535 and 8,795,506 which describe part of this silicon extraction technology. The authors declare no other conflicts of interest.

References

1. Woodhouse MA, Smith B, Ramdas A, Margolis RM. Crystalline Silicon Photovoltaic Module Manufacturing Costs and Sustainable Pricing: 1H 2018 Benchmark and Cost Reduction Road Map [Internet]. 2019 Feb [cited 2022 May 8] p. NREL/TP-6A20-72134, 1495719. Report No.: NREL/TP-6A20-72134, 1495719. Available from: http://www.osti.gov/servlets/purl/1495719/
2. Energy.gov [Internet]. [cited 2023 Apr 4]. Solar Photovoltaic Cell Basics. Available from: https://www.energy.gov/eere/solar/solar-photovoltaic-cell-basics
3. pv magazine International [Internet]. [cited 2022 May 8]. Polysilicon price fluctuations expected to continue until late 2023. Available from: https://www.pv-magazine.com/2022/02/24/polysilicon-price-fluctuations-expected-to-continue-until-late-2023/
4. pv magazine USA [Internet]. 2022 [cited 2022 May 8]. Polysilicon price reaches $39.3/kg — the highest since 2011. Available from: https://pv-magazine-usa.com/2022/02/23/polysilicon-price-reaches-39-3-kg-the-highest-since-2011/
5. Chigondo F (2018) From metallurgical-grade to solar-grade silicon: an overview. Silicon 10(3):789–798
6. Maurits JEA (2014) Chapter 2.6 - Silicon Production. In: Seetharaman S (ed) Treatise on Process Metallurgy [Internet]. Elsevier, Boston, pp 919–948 [cited 2022 May 8]. Available from: https://www.sciencedirect.com/science/article/pii/B9780080969886000225

7. Polysilicon Production: Siemens Process | Bernreuter Research [Internet]. [cited 2022 May 8]. Available from: https://www.bernreuter.com/polysilicon/production-processes/
8. Nohira T. Silicon Production by Molten Salt Electrolysis. In: Kreysa G, Ota K ichiro, Savinell RF, editors. Encyclopedia of Applied Electrochemistry [Internet]. New York, NY: Springer New York; 2014 [cited 2019 Oct 1]. p. 1963–6. Available from: http://link.springer.com/10.1007/978-1-4419-6996-5_457
9. Yasuda K, Nohira T (2022) Electrochemical production of silicon. High Temp Mater Process 41(1):247–278
10. Padamata SK, Saevarsdottir G (2023) Silicon electrowinning by molten salts electrolysis. Front Chem 11:1133990
11. Juzeliunas E, Fray DJ (2020) Silicon electrochemistry in molten salts. Chem Rev 120(3):1690–1709
12. Powell AC, Pal UB, Barriga S, Derezinski SJ, Earlam M. Clean, efficient metal electrolysis via SOM anodes [Internet]. Notice of Allowance * [cited 2019 Nov 15]. Available from: https://patents.google.com/patent/US20160376719A1/en
13. Pal UB, Powell AC (2007) The use of solid-oxide-membrane technology for electrometallurgy. JOM 59(5):44–49
14. Guan X, Pal UB, Jiang Y, Su S (2016) Clean metals production by solid oxide membrane electrolysis process. J Sustain Metall 2(2):152–166
15. Jiang Y, Xu J, Guan X, Pal UB, Basu SN (2013) Production of silicon by solid oxide membrane-based electrolysis process. MRS Proc 1493:231–235
16. Villalón T Jr (2018) Zero-direct emission silicon production via solid oxide membrane electrolysis [Internet] [Ph.D.]. Boston University, [Boston, MA, USA] Available from: https://hdl.handle.net/2144/30729
17. Ray HS (2006) Introduction to melts: molten salts, slags and glasses. Allied Publishers, p 39
18. COMSOL Multiphysics Reference Manual.
19. Moudgal A, Buasai S, Wu YJ, McMahon A, Hazerjian J, Luu V et al (2021) Finite element analysis and techno-economic modeling of solar silicon molten salt electrolysis. JOM 73(1). https://doi.org/10.1007/s11837-020-04468-y
20. Ibl N (1983 [cited 2023 Apr 5]. p. 239–315. (Comprehensive Treatise of Electrochemistry). Available from) Current Distribution. In: Yeager E, Bockris JO, Conway BE, Sarangapani S (eds) Comprehensive Treatise of Electrochemistry: Electrodics: Transport [Internet]. Springer US, Boston, MA. https://doi.org/10.1007/978-1-4615-6690-8_4
21. Dickinson EJF, Wain AJ (2020) The Butler-Volmer equation in electrochemical theory: origins, value, and practical application. J Electroanal Chem. 872:114145
22. Wouters MCHM, Eijkman HM, van Ruyven LJ (1976) The electrical conductivity of silicon between 500°C and 1200°C. Philips Res Repts 31:278–283
23. Horstemeyer MF Multiscale Modeling: A Review. In: Leszczynski J, Shukla MK (eds) Practical Aspects of Computational Chemistry: Methods, Concepts and Applications [Internet]. Springer Netherlands, Dordrecht. https://doi.org/10.1007/978-90-481-2687-3_4
24. Luo AA (2015) Material design and development: from classical thermodynamics to CALPHAD and ICME approaches. Calphad 50:6–22
25. Asadikiya M, Rudolf C, Zhang C, Boesl B, Zhong Y (2016) The Role of Calphad Approach in the Sintering of B4C with SIC as a Sintering Aid by Spark Plasma Sintering Technique. In: Additive Manufacturing and Strategic Technologies in Advanced Ceramics [Internet]. John Wiley & Sons, Ltd, pp 185–191. https://doi.org/10.1002/9781119236016.ch19
26. Andersson JO, Helander T, Höglund L, Shi P, Sundman B (2002) Thermo-Calc & DICTRA, computational tools for materials science. Calphad 26(2):273–312
27. Sundman B, Jansson B, Andersson JO (1985) The Thermo-Calc databank system. Calphad 9(2):153–190